THE JOURNAL OF PHYSICAL CHEMISTRY A

Article

pubs.acs.org/JPCA

Optical Emission from C_2^- Anions in Microwave-Activated CH_4/H_2 Plasmas for Chemical Vapor Deposition of Diamond

E. J. D. Mahoney,[†] B. S. Truscott,[†] M. N. R. Ashfold,*[,†] and Yu. A. Mankelevich*[,‡]

[†]School of Chemistry, University of Bristol, Bristol, U.K. BS8 1TS

[‡]Skobel'tsyn Institute of Nuclear Physics, Lomonosov Moscow State University, Leninskie gory, Moscow 119991, Russia

ABSTRACT: Visible emission from $C_2^-(B^2\Sigma_u^+)$ anions has been identified underlying the much stronger Swan band emission from neutral $C_2(d^3\Pi_g)$ radicals (henceforth C_2^-* and C_2*, respectively) in MW-activated C/H/(Ar) plasmas operating under conditions appropriate for the chemical vapor deposition (CVD) of diamond. Spatially resolved measurements of the C_2^-* and C_2* emissions as functions of the C/H/(Ar) ratio in the input gas mixture, the total pressure, and the applied MW power, together with complementary 2-D(r, z) plasma modeling, identifies dissociative electron attachment (DEA) to C_2H radicals in the hot plasma as the dominant source of the observed C_2^-* emission. Modeling not only indicates substantially higher concentrations of C_2H^- anions (from analogous DEA to C_2H_2) in the near-substrate region but also suggests that the anion number densities will typically be 3−4 orders of magnitude lower than those of the electrons and partner cations, i.e., mainly $C_2H_2^+$ and $C_2H_3^+$. The identification of negatively charged carbon-containing species in diamond CVD plasmas offers a possible rationale for previous reports that nucleation densities and growth rates can be enhanced by applying a positive bias to the substrate.

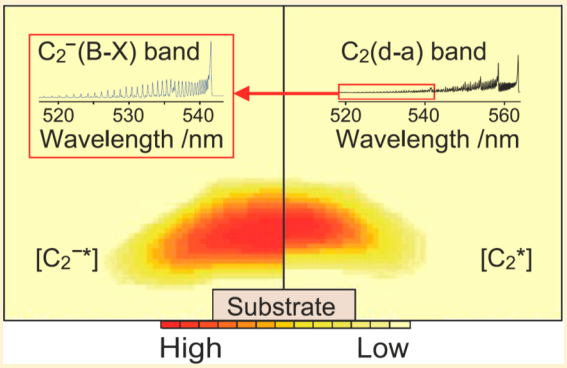

1. INTRODUCTION

Optical emission spectroscopy (OES) has found widespread use as a relatively straightforward and easy-to-implement probe of DC arc-jet[1−9] and microwave (MW)[10−59] plasmas used for the chemical vapor deposition (CVD) of diamond. Species amenable to study in this way in traditional dilute carbon/hydrogen (C/H) plasmas include electronically excited H atoms (via the Balmer emissions), H_2 molecules (typically via lines within the Fulcher system), and CH and C_2 radicals. To this list can be added electronically excited Ar atoms (when Ar is added to the process gas mixture),[1−3,10,12−14,16,18,21−24,26,28,31,33−37,39−42,44−48,50,54,56,57,60] B and BH (if a B-containing dopant is added),[39,44,58] CN and N_2 (when N_2 is present, either by design or as an impurity),[1,6,15,18,24−26,35,41,54,59] and OH and CO (when, for example, CO_2 is used as the carbon source).[25,27,43,49,51,55,57] The emitting species are generally formed by electron impact excitation (EIE) either of the corresponding ground-state species, or of a low-lying excited state in the case of C_2. Thus, the emission intensities are sensitive not just to the respective lower state populations but also to the electron temperature, T_e, and number density, n_e, and the variation of all of these quantities with changes in process conditions, e.g., in the gas composition and mixing ratio, total pressure p, applied MW power P, sign and magnitude of any substrate bias voltage, etc.,[6,7,9−11,13−16,18−24,26,27,29−31,34,36−46,48−60] and with location within the plasma volume. Several studies have investigated the correspondence (or otherwise) between measured OES intensities and absolute densities measured by absorption methods.[17,22,23,32,37,42,59] OES measurements made with high spectral resolution can provide estimates of the temperature of the emitting species, either through the measured Doppler broadening of a single spectral line (e.g., of the H Balmer-α line[14,16,17,22,28]) or from the relative intensities of a series of rotational lines in, for example, the emission spectrum of H_2[14,17] or C_2.[2,4,5,7,34,36,43,47,52,53,56] Given the typical pressures (and thus collision frequencies) prevailing in these plasmas, excited-state temperatures determined in this way are generally considered reliable proxies for the local gas temperature, T_{gas}.

Electron impact excitation is the dominant, but not the sole, mechanism by which emitting species arise in MW-activated gas mixtures used for diamond CVD. Spatially resolved measurements of both the BH radical emission in MW-activated B_2H_6/H_2(/Ar) gas mixtures and the CH and C_2 emissions from MW-activated $CH_4/CO_2/H_2$ plasmas[51] reveal chemiluminescence from these species, formed as products of exothermic atom−radical and radical−radical reactions, most clearly in regions of low electron density at the periphery of the plasma. Resonant collisional energy transfer from metastable triplet CO molecules in C/H/O plasmas has also been proposed as a contributor to the observed OH emission.[51]

Received: January 25, 2017
Revised: March 10, 2017
Published: March 20, 2017

DOI: 10.1021/acs.jpca.7b00814
J. Phys. Chem. A 2017, 121, 2760−2772

Here we report the first identification of optical emission from the electronically excited $C_2^-(B^2\Sigma_u^+)$ anion (henceforth C_2^-*) in a MW-activated C/H/(Ar) plasma operating under conditions appropriate for diamond CVD. To the best of our knowledge, this is the first charged species (anion or cation) to be observed by OES in such plasmas. The finding is noteworthy for several reasons. One centers on the C_2^-* production mechanism, which we deduce to be dissociative electron attachment (DEA) to the C_2H radical on the basis of plasma-chemical modeling. This modeling is informed by spatially resolved OES measurements comparing the variation of the optical emissions from C_2^-* and from neutral C_2 radicals in their $d^3\Pi_g$ state (henceforth C_2*) with the C/H/(Ar) ratio in the input process gas mixture, the total pressure, and the applied MW power. Second, the presence of anions may have implications for the detailed modeling of such plasmas. Previous analyses of MW-activated C/H/(Ar) containing plasmas[60,61] have assumed that the negatively charged particles partnering the cations (assumed to be mainly $C_2H_2^+$ and $C_2H_3^+$ in our previous work[60]) are exclusively electrons. Lastly, the presence of *negatively* charged carbon-containing species in diamond CVD plasmas offers a possible rationale for previous findings that nucleation densities and growth rates can be enhanced by applying not just a negative[62] but also a *positive*[31,40,63] bias voltage to the substrate.

2. EXPERIMENT

The experiments employ the previously described MW plasma-activated (PA) CVD reactor[64] with a new setup for imaging the optical emission from the plasma. Base conditions were chosen as P = 1.5 kW and p = 150 Torr, with flow rates $F(CH_4)$ = 19 standard cm^3 per minute (sccm) and $F(H_2)$ = 300 sccm (i.e., 6% CH_4 in H_2). Power, pressure, and $F(CH_4)$ were varied individually over the respective ranges $0.7 \le P \le 1.86$ kW, $50 \le p \le 275$ Torr, and $2 \le F(CH_4) \le 30$ sccm, while keeping the other parameters at their base values. The effect of adding Ar to the process gas mixture was investigated over the range $0 \le F(Ar) \le 60$ sccm, with $F(H_2)$ reduced in a compensatory way so as to ensure that $F(H_2)+F(Ar)$ = 300 sccm.

Optical emission from the plasma was coupled into a Czerny–Turner spectrograph (Newport MS127i) using a 250 mm focal length, f/16 objective lens and dispersed using an 1800 grooves mm^{-1} grating, yielding a spatial resolution of <0.5 mm and a spectral resolution of ≈0.11 nm (full width at half-maximum, fwhm) when a 13 μm entrance slit is used. The effects of adding Ar were investigated at lower spectral resolution (25 μm entrance slit) wherein, under base conditions, the recorded C_2*(0,0) and C_2^-*(0,0) emission intensities, henceforth $I_{em}(C_2$*) and $I_{em}(C_2^-$*), were both increased ∼2.5-fold. The diffracted radiation was imaged onto a cooled CCD detector (Andor Newton 970) with an overall spatial magnification of ≈0.1, and each image was scaled to the equivalent of a 2048 s. accumulation for direct comparability of the intensities. The lens aperture was closed right down in these studies, so the data reported here effectively include emission from the whole thickness of the plasma.

3. RESULTS AND DISCUSSION

3.1. Optical Emission Images and Spectral Analysis.

After a number of low-resolution survey scans, attention was concentrated on the wavelength range 489–566 nm, which under the present conditions is dominated by the $\Delta\nu = 0$ and $\Delta\nu = -1$ progressions of the $C_2(d^3\Pi_g - a^3\Pi_u)$ transition but also includes the much weaker $C_2^-(B^2\Sigma_u^+ - X^2\Sigma_g^+)$ $\Delta\nu = 0$ emission of current interest. The measured images comprise spatially and wavelength-resolved emission intensities $I_{em}(\lambda, z)$. Figure 1

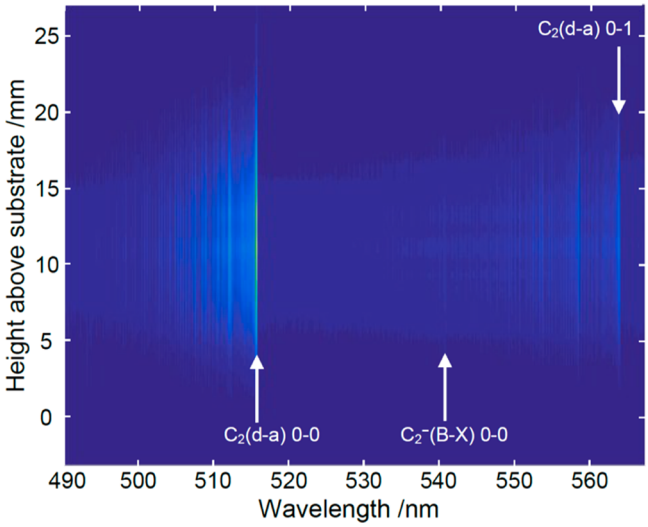

Figure 1. $I_{em}(\lambda,z)$ image (where z = 0 defines the substrate surface) in the wavelength range 489–566 nm from the plasma operating under base conditions: P = 1.5 kW, p = 150 Torr, $F(CH_4)$ = 19 sccm, and $F(H_2)$ = 300 sccm. Band heads associated with emitting C_2 and C_2^- species are indicated.

shows an illustrative image recorded under base conditions, after postprocessing to correct for vertical skew in the raw image. The height scale spans the range $-3 \le z \le 27$ mm, where z = 0 corresponds to the substrate surface and the scale is calibrated by imaging a test target placed at the substrate center position. The spectroscopic parameters for the $d^3\Pi_g$ and $a^3\Pi_u$ states of C_2[65] are known to sufficient precision that fitting to the C_2(d–a) line positions calculated using PGOPHER[66] constitutes the best means of calibrating the wavelength scale. From the $I_{em}(\lambda, z)$ images we can extract for further analysis one-dimensional (1-D) profiles showing $I_{em}(\lambda)$ at chosen z, or $I_{em}(z)$ for given λ. In doing so, we typically sum (i.e., bin) multiple rows or columns of the image, both to reduce the influence of noise in the resulting profile and limit the total number of profiles requiring to be analyzed.

Figure 2a shows the $I_{em}(\lambda)$ plot obtained by binning all intensity values measured for the range $9 \le z \le 12$ mm in the image shown in Figure 1, along with a best-fit simulation of the relevant part of the C_2(d–a) spectrum that assumes that each spectral feature is broadened with a Gaussian line shape having 0.11 nm fwhm. The fit returns a rotational temperature T_{rot} = 2900 K, in good accord with previous studies of such plasmas in this reactor,[42,59,64] and supports the assumption that the rotational population distribution in the emitting state is in local thermodynamic equilibrium. The (observed − calculated) difference plot over the limited wavelength range shown in Figure 2b highlights an obvious feature around 541.5 nm, which matches with the P-branch band-head of the $C_2^-(B^2\Sigma_u^+ - X^2\Sigma_g^+)$ (Herzberg–Lagerqvist system[67]) ($\nu' = 0 \rightarrow \nu'' = 0$) transition. The PGOPHER simulation of both this and the overlapping (1,1) band using the appropriate spectroscopic constants[68] and T_{rot} = 2900 K is shown in Figure 2c; nuclear spin statistics account for the absence of alternate lines in each branch. Many previous studies have reported optical emission

DOI: 10.1021/acs.jpca.7b00814
J. Phys. Chem. A 2017, 121, 2760–2772

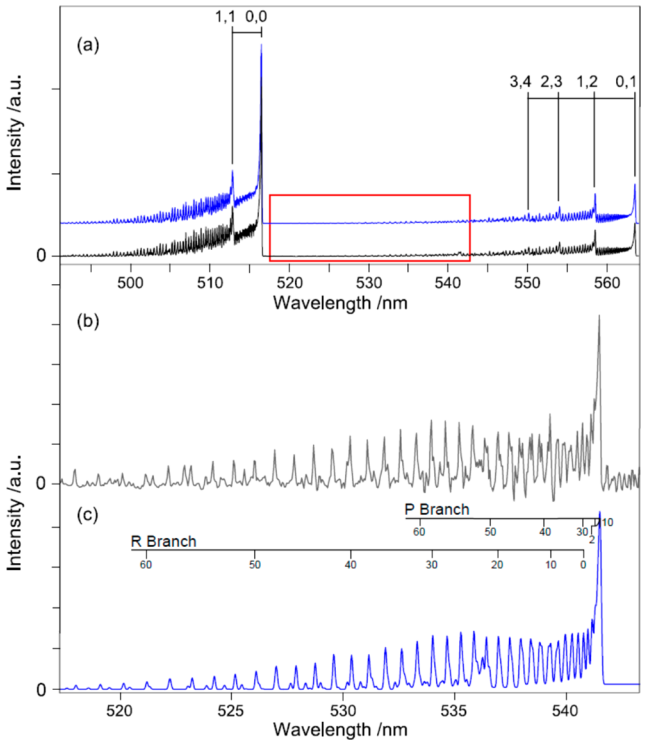

Figure 2. (a) $I_{em}(\lambda)$ (obs) plot of emission in the $9 \leq z \leq 12$ mm region of the image shown in Figure 1, along with a best-fit simulation (calc) of the relevant part of the C_2(d−a) spectrum and with the prominent band head (ν', ν'') assignments superposed. (b) Difference (i.e., obs − calc) plot on an expanded vertical scale showing the wavelength region bounded by the red box in (a). (c) shows a best-fit PGOPHER simulation of this C_2^-(B−X) (0,0) and (1,1) bands using the appropriate spectroscopic constants and assuming T_{rot} = 2900 K. Individual P and R branch lines within the origin band are labeled by their N'' quantum number.

in this spectral region from similar MW activated gas mixtures but, as far as we can see, none have been recorded with sufficient spectral resolution/signal−to−noise ratio or analyzed in sufficient detail to reveal the weak C_2^-* features.

Clearly, the difference plots are very sensitive to the high-v and high-J tail of the overlapping C_2(d−a) $\Delta v = -1$ progression, the appearance of which depends on T_{rot} (which, as before, is assumed to be a reliable measure of T_{gas}[60]). T_{gas} peaks in the core of the plasma and decreases both with increasing z and, more steeply, as $z \rightarrow 0$.[60] Much of the following analysis is based on the relative emission intensities $I_{em}(C_2^-*)$ and $I_{em}(C_2*)$, and their variation with spatial position and changes in process conditions. As it is important to separate the relative contributions from the two species as reliably as possible, we analyze the $I_{em}(\lambda)$ data using either Δz = 1.5 mm (higher spatial resolution) or Δz = 3 mm (lower resolution) vertical strips, each with its own best-fit T_{gas}. Under base conditions, for example, the higher resolution analysis shows $T_{gas} \approx 2750 \pm 20$ K at $z \approx 2.25$ mm, rising to a maximum of ≈2900 ± 20 K at $z \approx 11.25$ mm and declining again to ≈2640 ± 30 K at $z \approx 24.75$ mm. The comparative intensities presented below are normalized against the respective (0,0) bands in the best-fit PGOPHER simulations, with all other band intensities given by their relative transition probabilities and the vibrational partition function with $T_{vib} = T_{gas}$. To convert these intensities to relative excited-state populations requires scaling by the respective Einstein A-coefficients, for which we take 7.63×10^6 s^{-1} for the C_2(d−a) (0,0) band[65] and 9.1×10^6 s^{-1} for the C_2^-(B−X) (0,0) transition. This latter value was derived using literature values for the radiative lifetime of the B(ν'=0) level[68,69] and the relevant Franck−Condon factor.[70] Thus, if we consider the emission intensities as indicative of relative number densities, the values for $I_{em}(C_2^-*)$ given here should be reduced by a factor of 1.2 to obtain the relative excited-state number densities.

3.2. Trends in C_2* and C_2^-* Emission Intensities with Changes in Process Conditions. Figure 3 illustrates the similarity of the $I_{em}(C_2*)$ and $I_{em}(C_2^-*)$ profiles, analyzed at the higher spatial resolution, measured at pressures p = (a) 75, (b) 150, and (c) 225 Torr and otherwise base conditions. The respective profiles at any given p are similar, declining to near zero at small and large z. The maxima of both distributions shift to smaller z with increasing p, more noticeably in the case of

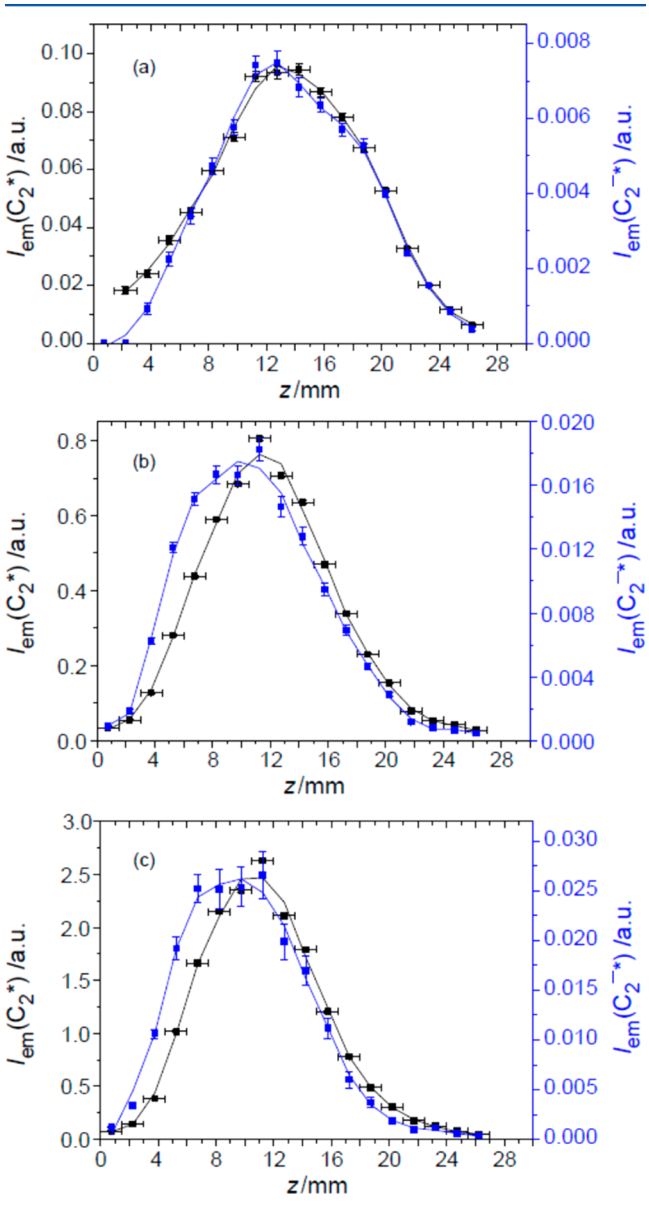

Figure 3. High-resolution (Δz = 1.5 mm) spatial profiles of $I_{em}(C_2*)$ and $I_{em}(C_2^-*)$ from a MW-activated CH_4/H_2 plasma operating at p = (a) 75, (b) 150 and (c) 225 Torr, with all other parameters held at base conditions.

DOI: 10.1021/acs.jpca.7b00814
J. Phys. Chem. A 2017, 121, 2760−2772

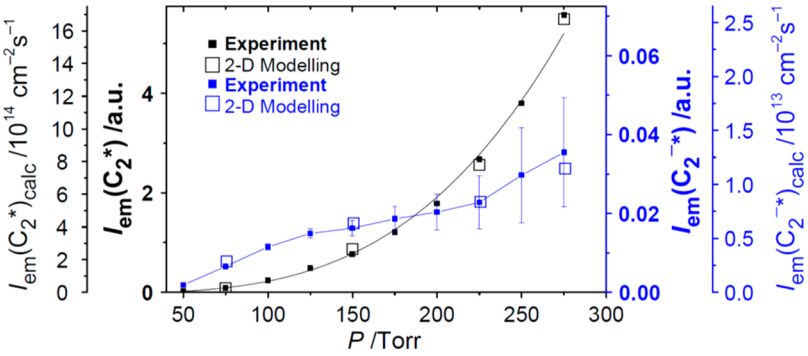

Figure 4. Solid symbols: variation in $I_{em}(C_2^*)$ and $I_{em}(C_2^{-*})$ intensities from the $9 \le z \le 12$ mm region from a MW-activated CH_4/H_2 plasma operating under base conditions of P, $F(CH_4)$, and $F(H_2)$, plotted as a function of total pressure over the range $50 \le p \le 275$ Torr. The intensities so derived have been reduced by a factor of 2 prior to display (on the inner y-axis scales) to allow direct comparison with the values shown in Figure 3. The solid line through the $I_{em}(C_2^*)$ data is a cubic p function, and the solid blue line simply connects the $I_{em}(C_2^{-*})$ data points. Open symbols: respective $I_{em}(C_2^*)_{calc}$ and $I_{em}(C_2^{-*})_{calc}$ emission rates (outer y-axis scales) returned by the 2-D modeling described in section 3.4.

$I_{em}(C_2^{-*})$, and the profiles visibly narrow. Closer inspection reveals that the ratio of emission intensities is a sensitive function of pressure. As Figure 4 shows, the C_2^* emission intensity observed from the $z = 10.5 \pm 1.5$ mm strip exhibits an approximate p^3 dependence, similar to that observed previously over a smaller range of pressures,[42] whereas $I_{em}(C_2^{-*})$ scales near-linearly with p. These data have been derived using the lower ($\Delta z = 3$ mm) spatial resolution, to minimize any effects from the peaks of the respective distributions shifting with p. The binned intensities so derived have then been halved prior to display to allow direct comparison with the intensities in the higher resolution ($\Delta z = 1.5$ mm) profiles shown in Figure 3b.

Panels a and b of Figure 5 show $I_{em}(C_2^*)$ and $I_{em}(C_2^{-*})$ profiles measured at $P = 0.9$ and 1.85 kW, respectively, with all other parameters maintained at their base values and analyzed at the higher ($\Delta z = 1.5$ mm) spatial resolution. As expected, reducing (increasing) P results in a smaller (larger) emitting volume, and again, the spatial distributions of the two emissions appear similar. Nonetheless, the $I_{em}(C_2^*)/I_{em}(C_2^{-*})$ ratio determined by (lower resolution) analysis of the $z = 10.5 \pm 1.5$ mm strip exhibits a marked P-dependence. This is quantified in Figure 6, which shows that (as with p, Figure 4) increasing P results in a near-cubic growth in $I_{em}(C_2^*)$, whereas $I_{em}(C_2^{-*})$ shows only a roughly linear increase. Again, the binned intensities have been halved prior to display for direct comparability with the intensities shown in Figures 3 and 5. The spectra also reveal a modest increase in T_{gas}, from ≈2830 K at $P = 0.7$ kW to ≈2920 K at $P = 1.85$ kW.

The final variables investigated were $F(CH_4)$ and $F(Ar)$. Figure 7 shows the variations in $I_{em}(C_2^*)$ and $I_{em}(C_2^{-*})$ determined by (lower resolution) analysis of the $z = 10.5 \pm 1.5$ mm strip when (a) $F(CH_4)$ varies across the range 2−30 sccm (or, in terms of input mole fractions, $0.66 \le X_0(CH_4) \le 9.1\%$) with all other parameters held at their base conditions, and (b) $F(Ar)$ varies over the range 0−60 sccm (input mole fractions $0 \le X_0(Ar) \le 18.8\%$), with $F(CH_4)$, p and P fixed at their base values. As Figure 7a shows, both emissions increase linearly at small $F(CH_4)$ and then somewhat less steeply at higher $F(CH_4)$. Figure 7b shows that adding Ar also results in (modest) increases in both $I_{em}(C_2^*)$ and $I_{em}(C_2^{-*})$, more so in the former case, such that the $I_{em}(C_2^*)/I_{em}(C_2^{-*})$ ratio increases from ≈40 at $X_0(Ar) = 0\%$ to ≈56 when $X_0(Ar) = 18.8\%$.

3.3. C_2^{-*} Formation Mechanism. We start by reprising some of the plasma characteristics established in our previous optical diagnosis and modeling studies of dilute CH_4/H_2 plasmas produced in this same CVD reactor at equivalent (base) power and pressure.[42,60,64] The supplied MW power is expended mainly on gas heating by rotational and vibrational excitation of H_2 and C_xH_y species by electrons driven in the MW field, with subsequent vibrational- and rotational-to-translational (V → T and R → T) energy redistribution, and by elastic collisions of electrons with atoms and molecules.[60,71] The gas temperature in the plasma core is $T_{gas} \approx 2900$ K, resulting in an $[H](r,z)$ distribution as shown in Figure 8a, a maximal H atom density $[H] \approx 4.4 \times 10^{16}$ cm^{-3}, and an H atom mole fraction $X(H) \approx 9.1\%$. These H atoms participate in

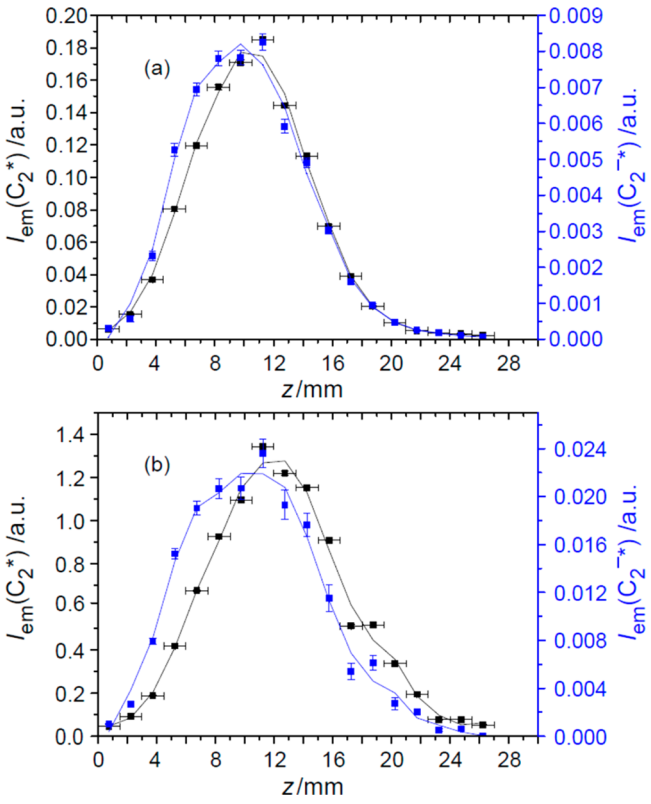

Figure 5. High-resolution ($\Delta z = 1.5$ mm) spatial profiles of $I_{em}(C_2^*)$ and $I_{em}(C_2^{-*})$ from a MW-activated CH_4/H_2 plasma operating $P =$ (a) 0.9 and (b) 1.85 kW, with all other parameters held at their base values.

DOI: 10.1021/acs.jpca.7b00814
J. Phys. Chem. A 2017, 121, 2760−2772

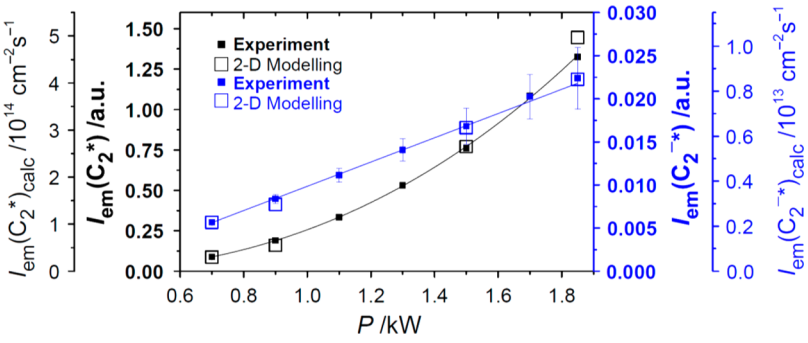

Figure 6. Solid symbols: variation in $I_{em}(C_2^*)$ and $I_{em}(C_2^{-*})$ intensities from the $9 \leq z \leq 12$ mm region from a MW-activated CH_4/H_2 plasma operating under base conditions of p, $F(CH_4)$, and $F(H_2)$, plotted as a function of applied power over the range $0.7 \leq P \leq 1.85$ kW. Again, the intensities so derived have been reduced by a factor of 2 prior to display (on the inner y-axis scales) to allow direct comparison with the values shown in Figures 3 and 5, and the solid black and blue lines show, respectively, cubic and linear p functions through the $I_{em}(C_2^*)$ and $I_{em}(C_2^{-*})$ data points. Open symbols: respective $I_{em}(C_2^*)_{calc}$ and $I_{em}(C_2^{-*})_{calc}$ emission rates (outer y-axis scales) returned by the 2-D modeling described in section 3.4.

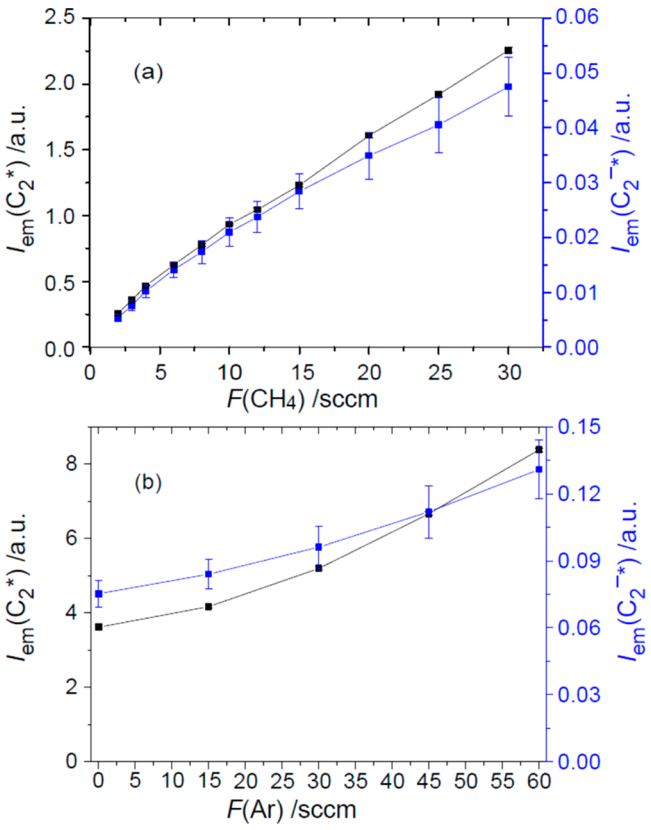

Figure 7. Variation in $I_{em}(C_2^*)$ and $I_{em}(C_2^{-*})$ intensities from the $9 \leq z \leq 12$ mm region from (a) a MW-activated CH_4/H_2 plasma operating under base conditions of P, p, and $F(H_2)$ plotted as a function of $F(CH_4)$, and (b) a MW-activated $CH_4/H_2/Ar$ plasma operating under base conditions of P, p, and $F(CH_4)$ plotted as a function of $F(Ar)$. Again, the intensities so derived have been reduced by a factor of 2 prior to display to allow direct comparison with the values shown in Figures 3 and 5, and the solid black and blue lines simply connect the $I_{em}(C_2^*)$ and $I_{em}(C_2^{-*})$ data points, respectively.

numerous H addition and abstraction reactions, summarized as a family of H-shifting equilibria that rapidly redistribute the input CH_4 into a whole range of CH_x ($x = 0-4$), C_2H_y ($y = 0-6$) and larger species, depending on the local T_{gas} and $X(H)$. C_2H_2 is the most stable carbon-containing species in the hot plasma region, and >97% of all the carbon in this region is predicted to be in the form of C_2H_2. Figure 8b shows the calculated electron density ($n_e(r,z)$) distribution; the peak electron density and temperature are, respectively, $n_e \approx 1.8 \times 10^{11}$ cm^{-3} and $T_e \approx 1.26$ eV. Both of these values are relatively flat across the plasma volume but fall steeply very close to the substrate and at large z and r. The radical species C_2H and, particularly, C_2 are concentrated in the hot plasma region, as illustrated by the 2-D(r,z) model outputs in Figure 8c,d. The dominant cations ensuring quasi-neutrality for our assumed ion chemistry are $C_2H_2^+$ and $C_2H_3^+$. The presence of anions has not been considered hitherto.

Several possible mechanisms for forming C_2^{-*} anions are now considered. The first involves electron attachment to neutral C_2, stabilized by the presence of a third body (M), i.e.

$$C_2 + e^- + M \rightarrow C_2^{-*} + M \quad (1)$$

The C_2 radical has a sufficiently large electron affinity (E_{ea} = 3.269 ± 0.006 eV[72]) to support bound excited states of the resulting anion, and the B state of C_2^- has a term value T_{00}(B–X) = 18484.03 cm^{-1} (2.29 eV).[68] Purely on energetic grounds, therefore, one could envisage that the emitting C_2^{-*} species observed in the present work arise directly from process 1. Such a mechanism might at first sight appear to be consistent with the similar spatial distributions of the C_2^* and C_2^{-*} emissions reported in Figures 3 and 5, but the very different p (Figure 4) and P (Figure 6) dependences of the respective emission intensities allow us to rule out reaction 1 as a major contributor to C_2^{-*} formation. Given the present plasma conditions, and even assuming a rather high value for the third-order recombination rate coefficient $k_1 > 10^{-29}$ cm^6 s^{-1}, reaction 1 would only be expected to make any discernible contribution to C_2^{-*} production for $p > 150$ Torr. The reverse collisional detachment reaction, with typical coefficient $k_{-1} = 7.5 \times 10^{-10} \times \exp(-11605/T_{gas})$,[73] is also not the main loss process for C_2^{-*}, as shown below.

Electron impact processes involving C_2^- and C_2^{-*} anions, i.e., the excitation/de-excitation reactions

$$C_2^- + e^- \rightleftharpoons C_2^{-*} + e^-$$

with rate coefficients $k_{EIE}(C_2^-) < k_{EIE}(C_2) \sim 10^{-9}$ cm^3 s^{-1} (ref 51), and the detachment/attachment reactions[74]

$$C_2^- + e^- \rightleftharpoons C_2 + 2e^-$$

are too slow to be important. The photoattachment process

$$C_2 + e^- \rightarrow C_2^{-*} \rightarrow C_2^- + h\nu \quad (2)$$

DOI: 10.1021/acs.jpca.7b00814
J. Phys. Chem. A 2017, 121, 2760–2772

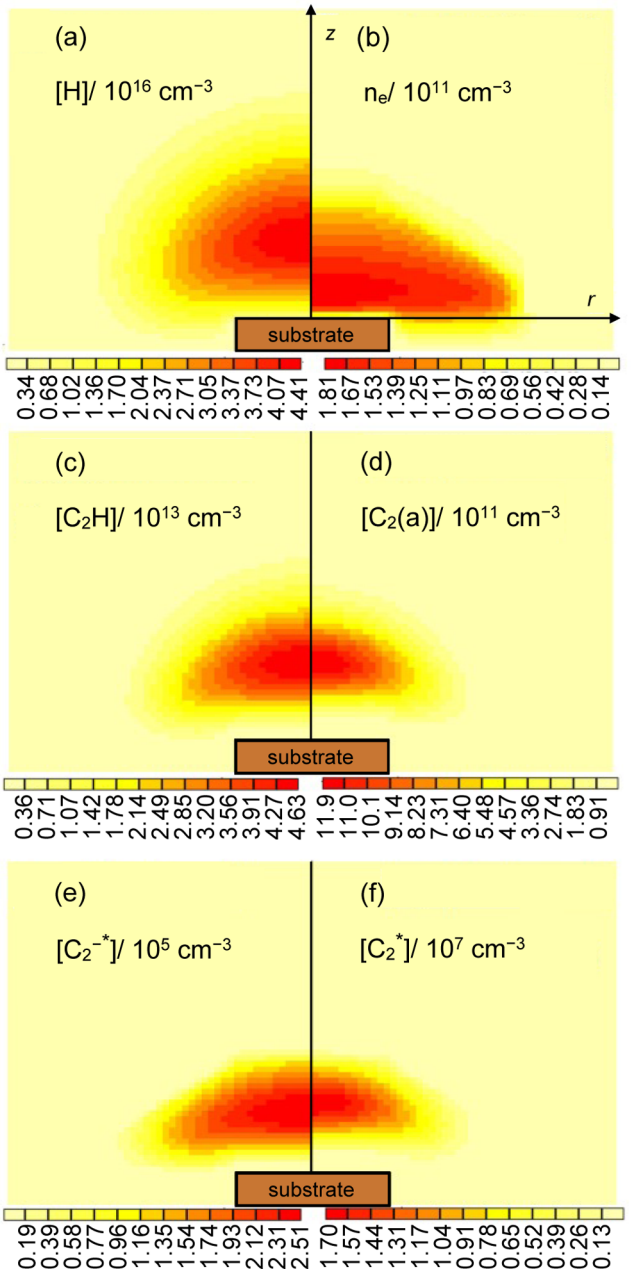

Figure 8. False color 2-D(r, z) plots showing the calculated number density distributions of (a) H, (b) n_e, (c) C_2H, (d) $C_2(a)$, (e) C_2^-*, and (f) C_2* from a MW-activated CH_4/H_2 plasma operating under base conditions. The vertical distance from the substrate to the quartz window at the top of the reactor is 5.7 cm, and the reactor radius is 6 cm.

can be excluded for similar reasons. Its estimated rate coefficient, $k_2 < 2 \times 10^{-15}(T_e/300)^{0.5}$ cm^3 s^{-1},[75] is too small for this reaction to be significant under the present process conditions.

As noted above, C_2H_2 is the dominant carbon-containing species in the hottest part of the plasma, so it is logical to consider possible C_2^-* production routes starting from C_2H_2. Although $T_e \approx 1.22 \pm 0.04$ eV under base conditions, the electron energy distribution function (EEDF) is not identically Maxwellian and possesses a heavy high-energy tail extending to >10 eV, as evidenced by the ubiquitous H Balmer emissions, which are excited by electron impact.[22,42] DEA to C_2H_2 has been investigated previously, with known channels yielding both C_2^- and C_2H^-:

$$C_2H_2 + e^- \rightarrow C_2^- + 2H \quad (3)$$

$$C_2H_2 + e^- \rightleftharpoons C_2H^- + H \quad (4)$$

The calculated threshold energy for the three-body fragmentation process (3) is 7.4 eV, but the first resonance in the DEA spectrum of C_2H_2 that yields C_2^- as the dominant product is centered at ≈8.1 eV, with a cross-section of 4.1 ± 1 pm^2.[76,77] Reaction 4 has a calculated threshold of 2.7 eV and a reported DEA cross-section of 3.6 ± 0.9 pm^2 at 2.95 eV, with C_2H^- as the dominant product. Combining the literature cross sections[76] with the EEDF calculated in our modeling allows estimation of rate coefficients for reactions 3 and 4, as functions of T_e under the present plasma conditions, as shown in Table 1. 2-D(r,z) coupled kinetic and transport modeling employing the previous C/H/(Ar) reaction mechanism,[60] supplemented by the additional reactions in Table 1, shows that reaction 3 is the main source of C_2^- close to the substrate ($0 < z < 5$ mm) and that reaction 4 is the main source of C_2H^- in the entire plasma region. Further processing of C_2H^- via H abstraction, followed by EIE, could then be envisaged as a means of generating the observed C_2^-* species, but the work of Barckholtz et al.[78] suggests that the reaction

$$C_2H^- + H \rightleftharpoons C_2^- + H_2$$

is rather slow ($k < 10^{-13}$ cm^3 s^{-1}). Thus, we conclude that H-shifting from C_2H^- cannot be an important source of C_2^-.

Processes 3 and 4 can also be ruled out as (indirect) sources of C_2^-* through consideration of the observed spatial distributions. The C_2H_2 number density (indicated using [ ] brackets, i.e., [C_2H_2]) increases at small z as an inevitable consequence of the fall in T_{gas} upon approaching the substrate.[60] The spatial distributions of the products of reactions 3 or 4 will closely resemble the product of the [C_2H_2] and n_e distributions, and the C_2H^- and C_2^- column densities (indicated using { } brackets) predicted on this basis peak close to the substrate and decline with increasing z as a result of the fall in, first, [C_2H_2] and, at larger z, n_e. Consequently, this predicted {$C_2^-(v''=0)$} distribution bears no resemblance to that of the $C_2(v''=0)$ neutrals, {$C_2(v''=0)$}, formed by the well-established[60] sequence of thermally driven H-shifting reactions. We emphasize that the contributions from reactions 3 and 4 still outweigh those from reactions 1 and 2 and are non-negligible C_2^- sources under the present conditions, but the observed spatial distributions allow us to exclude electron impact with the ground-state anion as the progenitor of the observed C_2^-* species.

Similar arguments will apply to any other formation processes starting from a stable precursor. For example, we have investigated the possible direct formation of C_2^-*

$$C_2H_2 + e^- \rightarrow C_2^-* + 2H \quad (3a)$$

proposed by Locht[79] to account for an increase in the cross-section for forming C_2^- ions in the DEA of C_2H_2 at incident electron energies ≥11.6 eV. Again, however, the {C_2^-*} distributions predicted assuming the participation of process 3a are very different from the present observations, particularly at low pressures (75 Torr) and powers (0.7 kW), where the inclusion of this reaction leads to very obvious enhancements in {C_2^-*} in the near-substrate region, in contradiction with the experimental measurements.

DOI: 10.1021/acs.jpca.7b00814
J. Phys. Chem. A 2017, 121, 2760−2772

Table 1. Anion Reactions: Rate Coefficients (in $cm^3\ s^{-1}$ Unless Explicitly Shown Otherwise) and Rates (in $cm^{-3}\ s^{-1}$, Calculated for Base Conditions at z = 10.5 and 1.5 mm, and r = 0) Used along with the Existing C/H/(Ar) Plasma Chemical Mechanism (ref 60) in Producing the Model Outputs Shown in Figure 9[a]

reaction	rate coefficient/$cm^3\ s^{-1}$ (if no other unit is indicated)	rate/$cm^{-3}\ s^{-1}$ z = 10.5 mm	rate/$cm^{-3}\ s^{-1}$ z = 1.5 mm	number
$C_2 + e^- + M \rightarrow C_2^-* + M$	$k_1 = 3 \times 10^{-29}\ cm^6\ s^{-1}$	2.33×10^{12}	1.05×10^{10}	(1)
$C_2^-* + M \rightarrow C_2 + e + M$	$k_{-1} = 7.5 \times 10^{-10} \times \exp(-11605/T_{gas})$	1.53×10^{12}	9.72×10^{9}	(−1)
$C_2H_2 + e^- \rightarrow C_2^- + H + H$	$k_3 = 2.28 \times 10^{-11} \times \exp(-93907/T_e)$	1.77×10^{13}	4.57×10^{13}	(3)
$C_2H_2 + e^- \rightarrow C_2H^- + H$	$k_4 = 4.62 \times 10^{-12} \times \exp(-34201/T_e)$	2.48×10^{14}	5.57×10^{14}	(4)
$C_2H^- + H \rightarrow C_2H_2 + e^-$	$k_{-4} = 1.6 \times 10^{-9}$	2.48×10^{14}	5.56×10^{14}	(−4)
$C_2H + e^- \rightarrow C_2^-* + H$	$k_5 = 1.9 \times 10^{-11} \times \exp(-34777/T_e)$	1.04×10^{13}	2.52×10^{11}	(5)
$C_2H + e^- \rightarrow C_2^- + H$	$k_6 = 3.87 \times 10^{-11} \times \exp(-20128/T_e)$	6.00×10^{13}	1.41×10^{12}	(6)
$C_2^-* + H \rightarrow C_2H + e^-$	$k_{-5} \approx 7.7 \times 10^{-10}$	7.92×10^{12}	1.13×10^{11}	(−5)
$C_2^- + H \rightarrow C_2H + e^-$	$k_{-6} = 7.7 \times 10^{-10}$	8.09×10^{13}	4.71×10^{13}	(−6)
$C_2^-* \rightarrow C_2^- + h\nu$	$A_7 = 1.3 \times 10^{7}\ s^{-1}$	3.26×10^{12}	1.40×10^{11}	(7)
$C_2 + e^- \rightarrow C_2* + e^-$	$k_8 = 10^{-8} \times \exp(-29065/T_e)$	1.96×10^{14}	5.88×10^{11}	(8)
$C_2* \rightarrow C_2 + h\nu$	$A_9 = 1.02 \times 10^{7}\ s^{-1}$	1.60×10^{14}	5.43×10^{11}	(9)
$C_2* + H_2 \rightarrow C_2H^\dagger + H$	$k_{10} = 1.5 \times 10^{-11} \times \exp(-3012/T_{gas})$	3.74×10^{13}	1.16×10^{11}	(10)

[a] T_e and T_{gas} in the exponents are in units of K (1 eV = 11605 K).

From here on, we therefore focus on electron-driven processes involving transient species—particularly the C_2H radical, which sits between C_2H_2 and C_2 in the sequence of H-shifting equilibria involving the C_2H_y (y = 0–6) family. As Figure 8c shows, its number density is predicted to peak at $[C_2H] \approx 5 \times 10^{13}\ cm^{-3}$ in the hot plasma region (i.e., to be ≈40-fold higher than $[C_2]$) and to adopt a more spatially extensive distribution than that of $C_2(a)$, which is given in Figure 8d. As we now show, adding the set of negative ion reactions listed in Table 1 to the C/H reaction mechanism used in our previous 2-D(r,z) coupled kinetic and transport modeling[60] enables near-quantitative replication of the measured $I_{em}(C_2^-*)$ and $I_{em}(C_2*)$ distributions, their relative intensities, and their respective variations with process conditions.

The dominant source of C_2^-* is deduced to be

$$C_2H + e^- \rightleftharpoons C_2^-* + H \quad (5)$$

with DEA also being the main source of ground-state C_2^- in the hot plasma core according to

$$C_2H + e^- \rightarrow C_2^- + H \quad (6)$$

The balance of reactions 5 and −5 and the radiative decay

$$C_2^-* \rightarrow C_2^- + h\nu \quad (7)$$

largely determine the C_2^-* concentration and thus the emission intensity, $I_{em}(C_2^-*)$. Other possible quenching processes, e.g., $C_2^-* + H_2 \rightarrow$ products, are unimportant relative to the reactive quenching process −5 under the present conditions.

In the quenching of C_2* species, however, the roles of H and H_2 are completely different. $I_{em}(C_2*)$ is modeled simply as the balance between EIE[51]

$$C_2 + e^- \rightarrow C_2* + e^- \quad (8)$$

radiative decay

$$C_2* \rightarrow C_2 + h\nu \quad (9)$$

and the quenching process $C_2* + H_2 \rightarrow$ products, e.g.

$$C_2* + H_2 \rightarrow C_2H^\dagger + H \quad (10)$$

where $C_2H^\dagger$ represents C_2H products possessing some, but undefined, internal excitation.

We have not found information on either the rates or the major products of reaction 10, which, as written, is exothermic by ≈3 eV. Pasternack et al.[80] reported a rate constant k_{-12} [$cm^3\ s^{-1}$] ≈ $1.5 \times 10^{-11} \exp(-3012/T_{gas})$ for the corresponding reaction of $C_2(a)$ radicals with H_2 (reaction −12 below) and, lacking alternative information, we have adopted a similar form for $k_{10}(T_{gas})$ in Table 1. The $C_2H^\dagger$ products are assumed to be rapidly quenched by H_2 and C_2H_2 with rate coefficients in the range $(0.5–1.5) \times 10^{-10}\ cm^3\ s^{-1}$ (ref 81), so reaction −10 is not considered to be a source of C_2*. Other possible C_2* loss processes such as the reactive quenching reaction

$$C_2* + H \rightarrow CH + H$$

for which we deduce a rate coefficient $k(T_{gas}) < 3.7 \times 10^{-12}\ cm^3\ s^{-1}$ from the coefficient of the reverse chemiluminescent reaction,[51] is too slow to be important under the prevailing plasma conditions. So, too, is the quenching of C_2* by CH_4 (with a reported rate coefficient $3.7 \times 10^{-11}\ cm^3\ s^{-1}$ at T_{gas} = 298 K) and other hydrocarbons.[82]

The rate coefficient for the associative detachment reaction −4 is due to Barckholtz et al.[78] We have not found reported DEA cross sections for reactions 5 and 6. The expression for k_5 was chosen to provide a value $k_5 \approx 1.5 \times 10^{-12}\ cm^3\ s^{-1}$ in the hot plasma region. Such a value, along with the appropriate rate coefficients k_8 and A_9 (Table 1), yields the calculated spatial distributions of C_2^-* and C_2* shown in Figure 8e,f, and the $\{C_2*(v'=0)\}$ and $\{C_2^-*(v'=0)\}$ column densities shown in Figure 9a. The respective profiles and the ratio of these column densities all match well with the measured $I_{em}(C_2*)$ and $I_{em}(C_2^-*)$ profiles and $I_{em}(C_2*)/I_{em}(C_2^-*)$ ratios. Changing the activation energy in the expression for k_5 has little impact on the predicted $\{C_2^-*(v'=0)\}$ profile. The rate coefficient k_6 is also not known, but its value is unimportant from the viewpoint of C_2^-* emission. Reaction 6 will contribute to C_2^- production but, as discussed above, C_2^- is not a significant source of the observed C_2^-* in the proposed mechanism.

One other aspect of the present data and its interpretation requires comment. The C_2^-* species are deduced to be formed directly by DEA to C_2H. The radiative lifetime of the $C_2^-(B)$ state is short (≈77 ns[69,70]), but more than an order of

DOI: 10.1021/acs.jpca.7b00814
J. Phys. Chem. A 2017, 121, 2760–2772

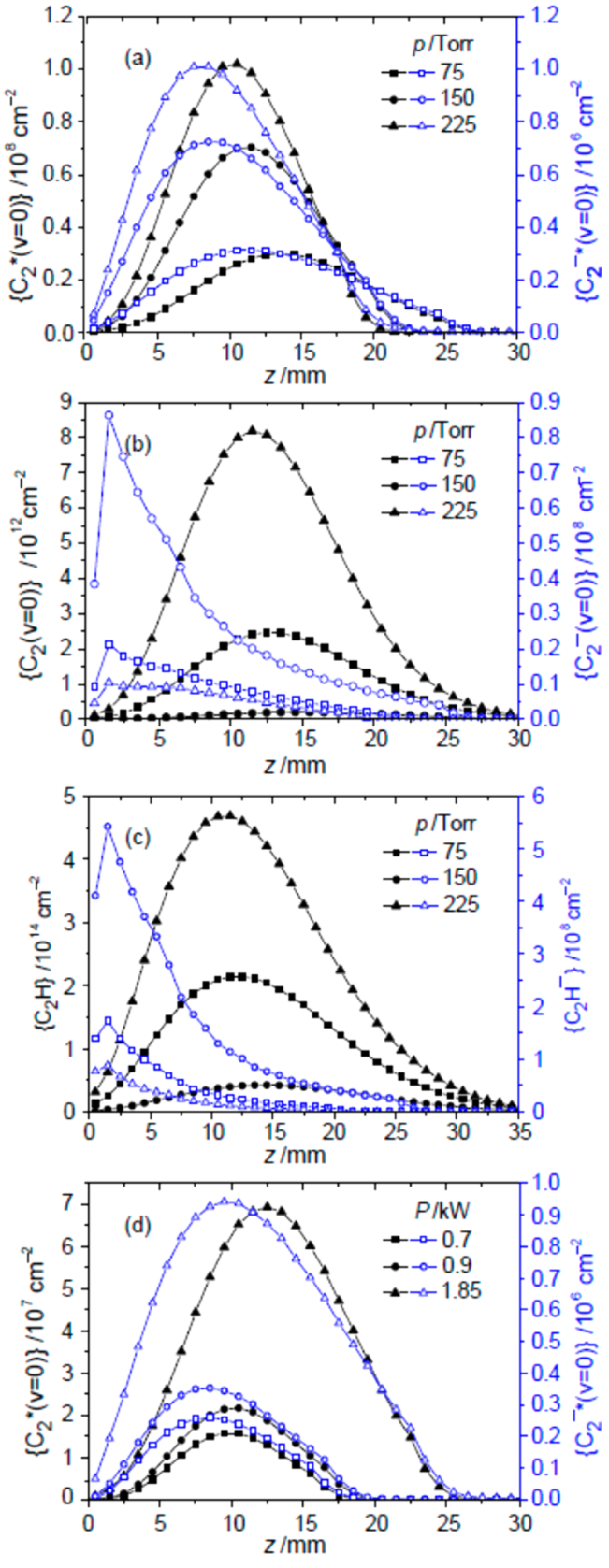

Figure 9. *z*-dependent column densities returned by the present 2-D modeling for (a) $\{C_2^*(v'=0)\}$ and $\{C_2^{-*}(v'=0)\}$ (left and right-hand *y*-axes respectively), (b) $\{C_2(v''=0)\}$ and $\{C_2^-(v''=0)\}$, and (c) $\{C_2H\}$ and $\{C_2H^-\}$, calculated for pressures p = 75, 150, and 225 Torr at constant power P = 1.5 kW. (d) shows the corresponding $\{C_2^*(v'=0)\}$ and $\{C_2^{-*}(v'=0)\}$ column density profiles for powers P = 0.7, 0.9, and 1.85 kW at constant p = 150 Torr. For the ease of visualization, the p = 75 and 150 Torr $\{C_2^*(v'=0)\}$ data in (a) have been multiplied by factors of 8 and 2, respectively, and the P = 0.7 and 0.9 kW data in (d) have been multiplied by factors of 4 and 3, respectively, prior to display. To compare with the observed $I_{em}(C_2^*)$ and $I_{em}(C_2^{-*})$ intensities (Figures 3 and 5), the column densities in (a) and (d) must be multiplied by the respective Einstein coefficients $A_9(v'=0\rightarrow v''=0)$ and $A_7(v'=0\rightarrow v''=0)$ (as in Figures 4 and 6 and described in section 3.4 and Table 2).

magnitude longer than the interval between collisions under the prevailing plasma conditions. Thus, the conclusion, from the spectral simulation (Figure 2b), that the C_2^{-*} species are in local thermodynamic equilibrium (LTE) is not wholly surprising. Rate coefficients for vibrational and, particularly, rotational relaxation of electronically excited molecules are typically higher than those for the corresponding ground-state species.[83] In our particular case, rotational-to-translational (R → T) energy relaxation of $C_2^{-*}(v',N')$ on H_2 is likely to be efficient. The fact that the light departing H atom formed in the DEA process is unlikely to generate a significant torque on the C_2^{-*} partner provides further reason why these anions show a rotational-state population distribution consistent with the rotational excitation of the C_2H precursor and thus the local T_{gas}. The C_2^{-*} vibrational-state population distribution ($C_2^{-*}(v')$) also appears to be in LTE. This may simply reflect a large (>10^{-10} cm^3 s^{-1}) V → T relaxation rate coefficient for C_2^{-*} in collision with H_2 but may also be a reflection of the very similar equilibrium C−C bond lengths in the $C_2H(X)$ radical (1.210 Å[84]) and in the B state of C_2^- (1.223 Å[67]), thereby ensuring only a vertical Franck−Condon contribution to the vibrational excitation.

The conclusion that reaction 3 is a dominant source of C_2^- near the substrate (Table 1) is key to explaining the very different profiles for C_2^{-*} and C_2^-, which are reflected in the respective calculated column densities (Figure 9a,b, respectively). In contrast, the spatial similarity of $I_{em}(C_2^{-*})$ and $I_{em}(C_2^*)$ (recall Figure 3) is understandable given the similar *z*-profiles calculated for $\{C_2H\}$, Figure 9c, and $\{C_2(v=0)\}$, Figure 9b, these being the dominant sources of the respective electron-induced emissions (i.e., DEA to C_2H (5) and EIE of C_2 (8), respectively). Reactive quenching of C_2^{-*} by H atoms, reaction (−5), and of C_2^* by H_2 molecules, reaction 10, also influences the calculated $\{C_2^*(v=0)\}/\{C_2^{-*}(v=0)\}$ ratios and, as we now show, can account for the major *p*- and *P*-dependent variations in the measured $I_{em}(C_2^*)/I_{em}(C_2^{-*})$ ratio.

3.4. Explaining the Process Condition Dependent Trends in $I_{em}(C_2^{-*})$ and $I_{em}(C_2^*)$. Analysis of the main C_2^* and C_2^{-*} production/loss reactions provides a rationale for the quite different dependences of $I_{em}(C_2^{-*})$ and $I_{em}(C_2^*)$ on both pressure and power (Figures 4 and 6).

$I_{em}(C_2^*)$. As noted above, C_2^* is produced by EIE of $C_2(a)$ (reaction 8), balanced by radiative decay (9) and reactive quenching (10); its number density will be given by an expression of the form

$$[C_2^*] \approx [C_2(a)] \times n_e \times k_8/(A_9 + k_{10}[H_2])$$

The steady-state concentration of $C_2(a)$ is established via fast, reversible H-shifting reactions

$$C_2H_2 + H \rightleftharpoons C_2H + H_2 \quad (11)$$

DOI: 10.1021/acs.jpca.7b00814
J. Phys. Chem. A 2017, 121, 2760−2772

$$C_2H + H \rightleftharpoons C_2(a) + H_2 \quad (12)$$

The aforementioned rate coefficient $k_{-12}(T_{gas})$[80] and thermochemical data were used in calculating the forward reaction coefficient $k_{12}(T_{gas}) \approx (7.05 \times 10^{-8}/T_{gas}) \times \exp(-8180/T_{gas})$. Balancing the direct and reverse H-shifting reactions 11 and 12 gives the following relation for $[C_2(a)]$:

$$[C_2(a)] \approx [C_2H] \times (k_{12}/k_{-12}) \times [H]/[H_2]$$
$$\approx [C_2H_2] \times (k_{11}/k_{-11}) \times (k_{12}/k_{-12}) \times ([H]/[H_2])^2$$

The calculated intensity $I_{em}(C_2^*)_{calc}$ (with units of cm^{-2} s^{-1}) is then the product $A_9(v'=0\rightarrow v''=0) \times \{C_2^*\}$, where $A_9(v'=0\rightarrow v''=0) = 7.63 \times 10^6$ s^{-1} (ref 65) and the column density $\{C_2^*\} \sim [C_2^*] \times 2R_{pl}$ (where $R_{pl}(z)$ is the plasma radius) has the following dependence as a result of reactions 8−12:

$$\{C_2^*\} \approx 2R_{pl} \times [C_2H_2] \times n_e \times (k_8/(A_9 + k_{10}[H_2]))$$
$$\times (k_{11}/k_{-11}) \times (k_{12}/k_{-12}) \times ([H]/[H_2])^2 \quad (13)$$

The 2-D model calculations show that the $[H]/[H_2]$ ratio in the plasma region is roughly proportional to both pressure and power, whereas the electron density n_e and temperature T_e depend only weakly on p and P. The maximal gas temperature T_{max} increases by a few percent with increasing p (the calculated $T_{max} \approx 2825$, 2890, 2920, and 2970 K at p = 75, 150, 225, and 275 Torr, respectively, at P = 1.5 kW) and P ($T_{max} \approx 2765$, 2890, and 2930 K at P = 0.7, 1.5, and 1.85 kW, respectively, at p = 150 Torr). $[C_2H_2]$ dominates the total carbon content and is thus proportional to the gas concentration and thus to p (if we neglect the weak variations in T_{max}). Radiative decay is dominant under the present conditions ($A_9/(k_{10}[H_2]) > 4$ under base conditions, Table 1). Equation 13 thus predicts a cubic pressure dependence $\{C_2^*\} \sim [C_2H_2] \times ([H]/[H_2])^2 \sim p^3$ at constant P, with weaker variations in R_{pl} (which decreases with p[59,85]) and in the product $(k_{11}/k_{-11}) \times (k_{12}/k_{-12})$ (which increases with p) largely compensating one another.

The 2-D modeling also rationalizes the observed near cubic power dependence of $\{C_2^*\}$. $[C_2H_2]$ is essentially independent of P. The $\{C_2^*\} \sim R_{pl} \times (k_{11}/k_{-11}) \times (k_{12}/k_{-12}) \times ([H]/[H_2])^2 \sim P^3$ dependence in this case relies on the same $([H]/[H_2])^2 \sim P^2$ contribution as above, supplemented by weaker, less than linear, increases in the ratio of the reaction coefficients $(k_{11}/k_{-11}) \times (k_{12}/k_{-12})$ (which increases as a result of the P-induced increase in T_{gas}) and in R_{pl} (which scales as $\sim P^{0.5}$ due the increased plasma volume, $V_{pl} \sim P$.[59,85])

$I_{em}(C_2^-*)$. A similar analysis of the main production/loss reactions for C_2^-* (reactions 5, −5, and 7) reveals a markedly different behavior for $I_{em}(C_2^-*)_{calc} \sim A_7(v'=0\rightarrow v''=0) \times \{C_2^-*\}$ when either pressure or power varies. This analysis uses $A_7(v'=0\rightarrow v''=0) = 9.1 \times 10^6$ s^{-1} and the following expression for $\{C_2^-*\} \sim [C_2^-*] \times 2R_{pl}$

$$\{C_2^-*\} \approx 2R_{pl} \times [C_2H_2] \times n_e \times k_5/(A_7 + k_{-5}[H])$$
$$\times (k_{11}/k_{-11}) \times ([H]/[H_2]) \quad (14)$$

The $[C_2H_2]/[H_2]$ ratio and n_e terms in eq 14 are largely insensitive to changes in P. Under base pressure conditions, the ratio $A_7/(k_{-5}[H])$ in the plasma core decreases from ≈0.83 at P = 0.7 kW, to ≈0.42 at P = 1.5 kW, and ≈0.34 at P = 1.85 kW. This equates to a ∼40% increase in the ratio $[H]/(A_7 + k_{-5}[H]) \sim P^{0.33}$ in this power range (from $0.55/k_{-5}$ at P = 0.7 kW up to $0.75/k_{-5}$ at P = 1.85 kW). This term, together with additional contributions from $R_{pl} \sim P^{0.5}$ and from the (k_{11}/k_{-11}) ratio, leads to a near−linear increase of $\{C_2^-*\}$ with P, as indeed observed for $I_{em}(C_2^-*)$ (Figure 6).

The pressure dependence of $\{C_2^-*\}$ in eq 14 is more complex. As in the case of $\{C_2*\}$, $[C_2H_2]$, and the $[H]/[H_2]$ ratio in the plasma region essentially scale with pressure, whereas n_e shows only a weak p-dependence. The $A_7/(k_{-5}[H])$ ratio in the plasma core decreases with increasing p, from ≈2 at p = 75 Torr, to ≈0.4 at p = 150 Torr, ≈0.18 at p = 225 Torr, and ≈0.12 at p = 275 Torr (all at P = 1.5 kW), which implies a clear $[H]$-dependence in eq 14. The $k_{-5}[H]$ term is relatively unimportant at low p but becomes the dominant term in the denominator at high pressures. R_{pl} also decreases with increasing p, as above.[84,85] Equation 14 thus predicts that $\{C_2^-*\}$ should show a (more than) linear increase with p at low p, but that the gradient of any such plot should decline to less than linear at higher p, in almost quantitative accord with the $I_{em}(C_2^-*)$ data shown in Figure 4 over the range $50 \le p \le 200$ Torr. Figure 4 suggests a further rise in $I_{em}(C_2^-*)$ at $p > 200$ Torr, though we caution that these data points carry progressively larger error bars. The present 2-D model calculations could accommodate such a trend by assuming a value $k_1 \approx 3 \times 10^{-29}$ cm^6 s^{-1} for the three-body reaction 1. Further speculation is unwarranted at this time, but we note that such a value lies well within the range ($\sim 10^{-31}$−10^{-28} cm^6 s^{-1}) reported for many other three-body electron attachments.[73,87] We also highlight that inclusion of the quenching reactions −5 within the overall mechanism is crucial for reproducing the diverse dependences of $I_{em}(C_2^-*)$ on p and P.

Comparisons between $I_{em}(C_2^-*)$ and $I_{em}(C_2*)$. Figures 3 and 5 consistently show the $I_{em}(C_2^-*)$ profile centered at slightly smaller z than the corresponding $I_{em}(C_2*)$ profile. This, too, is reproduced by the modeling, as seen in Figure 8e,f, and can be traced to the profiles of the respective parent species: $\{C_2H\}(z)$ is wider than $\{C_2(a)\}(z)$ (Figure 9c,b). That the $\{C_2^-*\}$ profile does not extend further on the high-z side reflects the spatial distribution of the H atoms, which act to quench C_2^-* according to reaction (−5). Consistent with Figure 8a, the maxima of $\{H\}(z)$ (and of $T_{gas}(z,r=0)$) under base conditions are at z = 12.5 mm, whereas the maximum of $\{C_2^-*\}(z)$ is located at z = 8.5 mm (Figure 9a). The proposed mechanism (Table 1) also reproduces the measured p- and P-dependent variations in the $I_{em}(C_2*)/I_{em}(C_2^-*)$ ratio well, as can be seen from the ratios of the calculated intensity maxima shown in Table 2.

Effects of Varying $F(CH_4)$ and $F(Ar)$. The functional dependences (13) and (14) derived above and our previous OES/actinometry,[42,51] CRDS,[42,64] and 2-D modeling studies[51,60] also enable explanations of the measured dependences of $I_{em}(C_2^-*)$ and $I_{em}(C_2*)$ when the input mole fractions of both methane, $X_0(CH_4)$, and argon, $X_0(Ar)$ are varied (Figure 7). Equations 13 and 14 show that $\{C_2*\}$ and $\{C_2^-*\}$ are both linearly proportional to $[C_2H_2]$ which, in turn, is proportional to $X_0(CH_4)$.[60] The other terms in eqs 13 and 14, e.g., $[H]$, the $[H]/[H_2]$ ratio, and T_e (which appears in k_5 and k_8 and has less direct influence on other plasma parameters like n_e), are barely changed by increasing the methane fraction in the range $0.66 \le X_0(CH_4) \le 9.09\%$ (as shown, for example, in Figure 3b of ref 42). Thus, we should predict a broadly linear increase in $I_{em}(C_2^-*)$ and $I_{em}(C_2*)$ (and a constant $I_{em}(C_2^-*)/I_{em}(C_2*)$ ratio) with increasing $X_0(CH_4)$, as observed (Figure 7a).

Figure 7b showed the corresponding trends observed when $X_0(Ar)$ varies in the range $0 \le X_0(Ar) \le 19\%$. $[C_2H_2]$ changes

DOI: 10.1021/acs.jpca.7b00814
J. Phys. Chem. A 2017, 121, 2760−2772

Table 2. *p*- and *P*-Dependent Variations in the $I_{em}(C_2^*)/I_{em}(C_2^{-*})$ Ratio Measured for the Strip Centered at z = 11.25 ± 0.75 mm Compared with the Corresponding Ratios of the Respective Maximum Intensities Calculated Using the Reaction Mechanism in Table 1

p/Torr	$\frac{I_{em}(C_2^*)}{I_{em}(C_2^{-*})}$ Figure 3	$\frac{A_9(v'=0\rightarrow v''=0)\times\{C_2^*\}_{max}}{A_7(v'=0\rightarrow v''=0)\times\{C_2^{-*}\}_{max}}$ Figure 9a
75	12	10
150	44	41
225	99	85
P/kW	$\frac{I_{em}(C_2^*)}{I_{em}(C_2^{-*})}$ Figures 5 and 6	$\frac{A_9(v'=0\rightarrow v''=0)\times\{C_2^*\}_{max}}{A_7(v'=0\rightarrow v''=0)\times\{C_2^{-*}\}_{max}}$ Figure 9d
0.7	16	13
0.9	22	17
1.85	57	62

little, but T_{gas}, T_e and, particularly, the $[H]/[H_2]$ ratio all increase with increasing X_0(Ar) (see, e.g., Figure 8 in ref 46). Given this increase in [H][42] and the inevitable decline in $[H_2]$ upon substitution by [Ar], the 2-D modeling predicts a steeper increase in $\{C_2^*\}$, which varies quadratically with $([H]/[H_2])^2$, eq 13, than in $\{C_2^{-*}\}$, which eq 14 shows to vary linearly with $[H]/[H_2]$. Again, such predictions agree with the present experimental findings. Combining the present predictions with previous experimental studies of Ar-rich plasmas,[46] we can predict much higher $\{C_2^*\}/\{C_2^{-*}\}$ ratios in, for example, the 0.5%CH_4/1%H_2/Ar mixtures used for depositing ultrananocrystalline diamond.

3.5. Further Implications for Plasma Activated Diamond CVD. C_2 is not the only radical species present in C/H plasmas that has a large electron affinity (E_{ea} = 3.269 ± 0.006 eV[72]). The electron affinity of C_2H is almost as large (E_{ea} = 2.969 ± 0.006 eV[72]), and that of the CN radical (which will be present if the plasma includes, whether by design or by accident, any nitrogen-containing precursor) is even larger (E_{ea} = 3.862 ± 0.004 eV[88]). Of the resulting anions, only C_2^- is an open-shell species, with bound excited electronic states capable of supporting OES in the visible spectral region. C_2H^- and CN^- are isoelectronic with N_2; their excited electronic states all lie at much higher energies, above the respective E_{ea} values. As Table 1 shows, the steady-state concentrations of anions like C_2^- and C_2H^- in a MW-activated C/H plasma are largely determined by DEA reactions 3, 4, and 6, balanced by associative attachment reactions −4 and −6. The rates of all other anion production and loss mechanisms (e.g., photoattachment, recombination with positive ions, electron detachment by electron impact, etc.) are orders of magnitude lower. As panels a, c, and d of Figure 9 show, the spatial profile of the C_2^{-*} anions revealed by OES is not representative of the majority anions. These are predicted to be $C_2H^-(\tilde{X})$, from reaction 4, supplemented by ground-state C_2^- anions from reactions 3 and 6. The column densities of these ground-state anions are predicted to peak at small $z \approx 1.5$ mm, as with the main cations ($C_2H_2^+$ and $C_2H_3^+$), but to be 3−4 orders of magnitude smaller than those of the cations under base conditions.

We can also predict (perhaps surprisingly) high abundances of CN^- anions in the case of N-containing C/H plasmas. As shown in our recent combined experimental and modeling studies of MW and DC activated $CH_4/N_2/H_2$ plasmas, HCN is by far the most abundant N containing species (besides N_2) in the near substrate region.[59,86] DEA to HCN, i.e.

$$HCN + e^- \rightleftharpoons CN^- + H \quad (15)$$

has a huge cross-section at near threshold energies (reaching 940 pm^2 at incident electron energies ≈1.85 eV), attributable to a $^2\Pi$ shape resonance.[89] Combining the reported cross-section with the calculated EEDF translates into a dissociative attachment coefficient $k_{15} \sim 2 \times 10^{-10}$ cm^3 s^{-1}. This coefficient, and an associative detachment coefficient $k_{-15} \sim 6.3 \times 10^{-10}$ cm^3 s^{-1} (from ref 90), allows us to predict number densities $[CN^-] \sim 10^8$ cm^{-3} (cf. neutral $[CN] \sim 10^9$ cm^{-3}) in the near substrate region and $[CN^-] \sim 10^7$ cm^{-3} (cf. $[CN] \sim 10^{11}$ cm^{-3}) in the plasma core for the base 4%CH_4/0.6%N_2/H_2 plasma considered in our recent study.[59] Extrapolating to lower N_2 input mole fractions, even with $X_0(N_2)$ = 100 ppm, we predict that CN^- anions from process 15 could account for ∼5% of the total near substrate anion concentration (which will then be dominated by $[C_2H^-] < 3 \times 10^7$ cm^{-3} from process 4). We reiterate, however, that this anion number density is still 3 or more orders of magnitude lower than the concentrations of electrons and the positive ions $n_e \sim \sum[C_xH_y^+] \sim 10^{11}$ cm^{-3}.

Negative bias enhanced nucleation (BEN) has long been recognized as a route to accelerating diamond film growth on silicon substrates[62] and is generally rationalized in terms of impacting C/H-containing cations yielding an interfacial SiC layer that facilitates subsequent diamond growth.[91−94] The present identification of C_2^{-*} anions in a MW activated C/H plasma typical of those used for diamond CVD, and the deduction that other anions (e.g., C_2H^-, and CN^- in the presence of adventitious N_2) must also be present in the near substrate region, offer a plausible explanation for the (fewer) previous reports[31,40,63] that the application of a *positive* bias voltage to the substrate can also lead to enhanced nucleation densities and growth rates. Negative BEN exploits the majority ions: as shown above, the cation densities in these plasmas are several orders of magnitude higher than those of the anions. But the dominant anions identified in the present work have much higher average C:H ratios, which may be beneficial for developing a carbon-rich seed layer.

4. CONCLUSIONS

Electronically excited C_2^{-*} anions have been identified, by spatially resolved imaging of their optical emission, in a MW-activated C/H/(Ar) plasma operating under conditions appropriate for diamond CVD. Various possible formation mechanisms have been modeled, only one of which (DEA to C_2H resulting in direct formation of the observed C_2^{-*} anions, balanced by the inverse associative detachment process) is consistent with the observed spatial distributions and the measured variations in emission intensity with the C/H/(Ar) ratio in the process gas mixture, the total pressure, and the applied MW power. The same 2-D(r,z) plasma-chemical modeling predicts DEA to C_2H_2 as a yet more important source of (C_2H^-) anions in such plasmas, and DEA to HCN as an efficient route to forming CN^- anions when a nitrogen-containing precursor is present. This work thereby extends previous analyses of such MW-activated diamond CVD plasmas that assume the charged particles to be exclusively cations and electrons. Although the predicted anion densities never exceed 0.1% of the cation density under any conditions investigated, their newly confirmed presence may offer some rationale for

DOI: 10.1021/acs.jpca.7b00814
J. Phys. Chem. A 2017, 121, 2760−2772

previous findings that nucleation densities and diamond growth rates can be enhanced by using a positive substrate bias.

AUTHOR INFORMATION

Corresponding Authors

*M. N. R. Ashfold. E-mail: mike.ashfold@bris.ac.uk.

*Y. A. Mankelevich. E-mail: ymankelevich@mics.msu.su.

ORCID

M. N. R. Ashfold: 0000-0001-5762-7048

Notes

The authors declare no competing financial interest.

All underlying experimental data are openly available at https://data.bris.ac.uk/data/dataset/mqk43szimid014npfya8ejxyr.

ACKNOWLEDGMENTS

The Bristol authors are grateful for financial support from the Engineering and Physical Sciences Research Council (EPSRC) through grant no. EP/K018388/1, the EPSRC Centre for Doctoral Training in Diamond Science and Technology (EP/L015315/1), and Element Six Ltd. The authors are also grateful for the many and varied contributions from colleagues Drs. Colin Western and James Smith. The work was performed within the Cooperation in Science and Technology Agreement between Lomonosov Moscow State University, Skobeltsyn Institute of Nuclear Physics, and the University of Bristol.

REFERENCES

(1) Reeve, S. W.; Weimer, W. A. Plasma Diagnostics of a DC Arcjet Chemical-Vapor-Deposition Diamond Reactor. *Thin Solid Films* **1993**, *236*, 91−95.

(2) Reeve, S. W.; Weimer, W. A. Plasma Diagnostics of a Direct-Current Arcjet Diamond Reactor. 2. Optical-Emission Spectroscopy. *J. Vac. Sci. Technol., A* **1995**, *13*, 359−367.

(3) Yamaguchi, H.; Ishii, M.; Uematsu, K.; Morimoto, S. Characterisation of a DC Arcjet Plasma for Diamond Growth by Measurement of Spatial Distributions of Optical Emission. *Jpn. J. Appl. Phys. Pt. 1* **1996**, *35*, 2306−2313.

(4) Brinkman, E. A.; Raiche, G. A.; Brown, M. S.; Jeffries, J. B. Optical Diagnostics for Temperature Measurement in a DC Arcjet Reactor used for Diamond Deposition. *Appl. Phys. B: Lasers Opt.* **1997**, *64*, 689−697.

(5) Luque, J.; Juchmann, W.; Brinkman, E. A.; Jeffries, J. B. Excited State Density Distributions of H, C, C_2 and CH by Spatially Resolved Optical Emission in a Diamond Depositing DC-Arcjet Reactor. *J. Vac. Sci. Technol., A* **1998**, *16*, 397−408.

(6) Smith, J. A.; Rosser, K. N.; Yagi, H.; Wallace, M. I.; May, P. W.; Ashfold, M. N. R. Diamond Deposition in a DC-Arc Jet CVD System: Investigations of the Effects of Nitrogen Addition. *Diamond Relat. Mater.* **2001**, *10*, 370−375.

(7) Wills, J. B.; Smith, J. A.; Boxford, W. E.; Elks, J. M. F.; Ashfold, M. N. R.; Orr-Ewing, A. J. Measurements of C_2 and CH Concentrations and Temperatures in a DC Arc Jet using Cavity Ring Down Spectroscopy. *J. Appl. Phys.* **2002**, *92*, 4213−4222.

(8) Chen, G. C.; Li, B.; Li, H.; Han, X. Q.; Hei, L. F.; Song, J. H.; Li, C. M.; Tang, W. Z.; Lu, F. X. In situ Observation of Nucleation by Optical Emission Spectra in CVD Diamond. *Diamond Relat. Mater.* **2010**, *19*, 15−20.

(9) Zheng, S.-J.; Ding, F.; Xie, X.-H.; Tang, Z.-L.; Zhang, Y.-C.; Li, H.; Yang, K.; Zhu, X.-D. A Diagnosis of Gas-Phase Processes in a High Pressure DC CH_4/H_2 Plasma. *Acta. Phys. Sinica* **2013**, *62*, 165204.

(10) Shigesato, Y.; Boekenhauer, R. E.; Sheldon, B. W. Emission-Spectroscopy During Direct-Current-Biased, Microwave-Plasma Chemical-Vapor-Deposition of Diamond. *Appl. Phys. Lett.* **1993**, *63*, 314−316.

(11) Gruen, D. M.; Liu, S. Z.; Krauss, A. R.; Pan, X. Z. Buckyball Microwave Plasmas − Fragmentation and Diamond-Film Growth. *J. Appl. Phys.* **1994**, *75*, 1758−1763.

(12) Beckmann, R.; Sobisch, B.; Kulisch, W.; Rau, C. Investigation of the Bias Nucleation Process in Microwave Plasma-Enhanced Chemical-Vapor-Deposition of Diamond. *Diamond Relat. Mater.* **1994**, *3*, 555−559.

(13) Tixier, C.; Tristant, P.; Desmaison, J.; Merle, D. Remote Microwave Plasma-Enhanced Chemical-Vapor-Deposition of Amorphous-Carbon − Optical Emission Spectroscopy Characterisation of the Afterglow and Growth-Rates. *J. Phys. IV.* **1995**, *5*, 593−600.

(14) Lang, T.; Stiegler, J.; von Kaenel, Y.; Blank, E. Optical Emission Diagnostics and Film Growth during Microwave-Plasma-Assisted Diamond CVD. *Diamond Relat. Mater.* **1996**, *5*, 1171−1184.

(15) Vandevelde, T.; Nesladek, M.; Quaeyhaegens, C.; Stals, L. Optical Emission Spectroscopy of the Plasma During CVD Diamond Growth with Nitrogen Addition. *Thin Solid Films* **1996**, *290−291*, 143−147.

(16) Gicquel, A.; Chenevier, M.; Breton, Y.; Petiau, M.; Booth, J. P.; Hassouni, K. Ground State and Excited State H-Atom Temperatures in a Microwave Plasma Diamond Deposition Reactor. *J. Phys. III* **1996**, *6*, 1167−1180.

(17) Gicquel, A.; Hassouni, K.; Breton, Y.; Chenevier, M.; Cubertafon, J. C. Gas Temperature Measurements by Laser Spectroscopic Techniques and by Optical Emission Spectroscopy. *Diamond Relat. Mater.* **1996**, *5*, 366−372.

(18) Barshilia, H. C.; Mehta, B. R.; Vankar, V. D. Optical Emission Spectroscopy during the Bias-Enhanced Nucleation of Diamond Microcrystals by Microwave Plasma Chemical Vapor Deposition Process. *J. Mater. Res.* **1996**, *11*, 2852−2860.

(19) Whitfield, M. D.; Rodway, D.; Savage, J. A.; Foord, J. S.; Jackman, R. B. Bias-Enhanced Nucleation of Diamond on Metals: an OES and Electrical Investigation. *Diamond Relat. Mater.* **1997**, *6*, 658−663.

(20) Chen, Y. H.; Hu, C. T.; Lin, I. N. Selected-Area Deposition of Diamond Films on Silicon-Nitride-Coated Silicon Substrates using Negatively Biased Microwave Plasma Enhanced Chemical Vapor Deposition Technique. *Jpn. J. Appl. Phys. Pt. 1.* **1997**, *36*, 6900−6904.

(21) Han, Y. S.; Kim, Y. K.; Lee, J. Y. Effects of Argon and Oxygen Addition to the CH_4-H_2 Feed Gas on Diamond Synthesis by Microwave Plasma Enhanced Chemical Vapor Deposition. *Thin Solid Films* **1997**, *310*, 39−46.

(22) Gicquel, A.; Chenevier, M.; Hassouni, K.; Tserepi, A.; Dubus, M. Validation of Actinometry for Estimating Relative Hydrogen Atom Densities and Electron Energy Evolution in Plasma Assisted Diamond Deposition Reactors. *J. Appl. Phys.* **1998**, *83*, 7504−7521.

(23) Goyette, A. N.; Lawler, J. E.; Anderson, L. W.; Gruen, D. M.; McCauley, T. G.; Zhou, D.; Krauss, A. R. C_2 Swan Band Emission Intensity as a Function of C_2 Density. *Plasma Sources Sci. Technol.* **1998**, *7*, 149−153.

(24) Goyette, A. N.; Lawler, J. E.; Anderson, L. W.; Gruen, D. M.; McCauley, T. G.; Zhou, D.; Krauss, A. R. Spectroscopic Determination of Carbon Dimer Densities in Ar-H_2-CH_4 and Ar-H_2-C_{60} Plasmas. *J. Phys. D: Appl. Phys.* **1998**, *31*, 1975−1986.

(25) Bougdira, J.; Remy, M.; Alnot, P.; Bruch, C.; Kruger, J. K.; Chatei, H.; Derkaoui, J. Combined Effect of Nitrogen and Pulsed Microwave Plasma on Diamond Growth using CH_4-CO_2 Gas Mixture. *Thin Solid Films* **1998**, *325*, 7−13.

(26) Vandevelde, T.; Wu, T. D.; Quaeyhaegens, C.; Vlekken, J.; D'Olieslaeger, M.; Stals, L. Correlation Between the OES Plasma Composition and the Diamond Film Properties during Microwave PA-CVD with Nitrogen Addition. *Thin Solid Films* **1999**, *340*, 159−163.

(27) Elliott, M. A.; May, P. W.; Petherbridge, J.; Leeds, S. M.; Ashfold, M. N. R.; Wang, W. N. Optical Emission Spectroscopic Studies of Microwave Enhanced Diamond CVD using CH_4/CO_2 Plasmas. *Diamond Relat. Mater.* **2000**, *9*, 311−316.

(28) Gicquel, A.; Silva, F.; Hassouni, K. Diamond Growth Mechanisms in Various Environments. *J. Electrochem. Soc.* **2000**, *147*, 2218−2226.

DOI: 10.1021/acs.jpca.7b00814
J. Phys. Chem. A 2017, 121, 2760−2772

(29) Khachan, J.; James, B. W.; Marfoure, A. Effect of Repetition Rate of a Pulsed Microwave Diamond Forming Plasma on the Density of C_2. *Appl. Phys. Lett.* **2000**, *77*, 2973−2975.
(30) Chen, L. C.; Kichambare, P. D.; Chen, K. H.; Wu, J. J.; Yang, J. R.; Lin, S. T. Growth of Highly Transparent Nanocrystalline Diamond Films and a Spectroscopic Study of the Growth. *J. Appl. Phys.* **2001**, *89*, 753−759.
(31) Chiang, M. J.; Hon, M. H. Positive DC Bias-Enhanced Nucleation with High CH_4 Concentration. *Diamond Relat. Mater.* **2001**, *10*, 1470−1476.
(32) John, P.; Rabeau, J. R.; Wilson, J. I. B. The Cavity Ring-Down Spectroscopy of C_2 in a Microwave Plasma. *Diamond Relat. Mater.* **2002**, *11*, 608−611.
(33) Lamara, T.; Belmahi, M.; Bougdira, J.; Benedic, F.; Henrion, G.; Remy, M. Diamond Thin Film Growth by Pulsed Microwave Plasma at High Power Density in a CH_4/H_2 Gas Mixture. *Surf. Coat. Technol.* **2003**, *174*, 784−789.
(34) Mortet, V.; Hubicka, Z.; Vorlicek, V.; Jurek, K.; Rosa, J.; Vanecek, M. Diamond Growth by Microwave Plasma Enhanced Chemical Vapour Deposition: Optical Emission Characterisation and Effect Argon Addition. *Phys. stat. Sol. (a)* **2004**, *201*, 2425−2431.
(35) Rabeau, J. R.; John, P.; Wilson, J. I. B.; Fan, Y. The Role of C_2 in Nanocrystalline Diamond Growth. *J. Appl. Phys.* **2004**, *96*, 6724−6732.
(36) Lombardi, G.; Bénédic, F.; Mohasseb, F.; Hassouni, K.; Gicquel, A. Determination of Gas Temperature and C_2 Absolute Density in $Ar/H_2/CH_4$ Microwave Discharges used for Nanocrystalline Diamond Deposition from the C_2 Mulliken System. *Plasma Sources Sci. Technol.* **2004**, *13*, 375−386.
(37) Griffin, J.; Ray, P. C. Role of Inert Gas in the Low-Temperature Nanodiamond Chemical Vapour Deposition Process. *Nanotechnology* **2006**, *17*, 1225−1229.
(38) Su, C.-H.; Chang, C. Y. Effect of CH/C_2 Species Density on Surface Morphology of Diamond Film Grown by Microwave Plasma Jet Chemical Vapor Deposition. *Mater. Trans.* **2008**, *49*, 1380−1384.
(39) Rayar, M.; Supiot, P.; Veis, P.; Gicquel, A. Optical Emission Study of a Doped Diamond Deposition Process by Plasma Enhanced Chemical Vapor Deposition. *J. Appl. Phys.* **2008**, *104*, 033304.
(40) Chiang, M. J.; Hon, M. H. Optical Emission Spectroscopy Study of Positive Direct Current Bias Enhanced Diamond Nucleation. *Thin Solid Films* **2008**, *516*, 4765−4770.
(41) Liang, Q.; Chin, C. Y.; Lai, J.; Yan, C.-s.; Meng, Y.; Mao, H.-k.; Hemley, R. J. Enhanced Growth of High Quality Single Crystal Diamond by Microwave Plasma Assisted Chemical Vapor Deposition at High Gas Pressures. *Appl. Phys. Lett.* **2009**, *94*, 024103.
(42) Ma, J.; Ashfold, M. N. R.; Mankelevich, Y. A. Validating Optical Emission Spectroscopy as a Diagnostic of Microwave Activated $CH_4/Ar/H_2$ Plasmas used for Diamond Chemical Vapor Deposition. *J. Appl. Phys.* **2009**, *105*, 043302.
(43) Gries, T.; Vandenbulcke, L.; de Persis, S.; Aubry, O.; Delfau, J. L. Diagnostics and Modelling of CH_4/CO_2 Plasmas for Nanosmooth Diamond Deposition: Comparison to Experimental Data. *J. Vac. Sci. Technol. B* **2009**, *27*, 2309−2320.
(44) Ma, J.; Richley, J. C.; Davies, D. R. W.; Ashfold, M. N. R.; Mankelevich, Y. A. Spectroscopic and Modelling Investigations of the Gas Phase Chemistry and Composition in Microwave Plasma Activated $B_2H_6/CH_4/Ar/H_2$ Mixtures. *J. Phys. Chem. A* **2010**, *114*, 10076−10089.
(45) Lin, I.-N.; Chen, H.-C.; Wang, C.-S.; Lee, Y.-R.; Lee, C.-Y. Nanocrystalline Diamond Microstructures from $Ar/H_2/CH_4$-Plasma Chemical Vapour Deposition. *CrystEngComm* **2011**, *13*, 6082−6089.
(46) Richley, J. C.; Fox, O. J. L.; Ashfold, M. N. R.; Mankelevich, Y. A. Combined Experimental and Modelling Studies of Microwave Activated $CH_4/H_2/Ar$ Plasmas for Microcrystalline, Nanocrystalline, and Ultrananocrystalline Diamond Deposition. *J. Appl. Phys.* **2011**, *109*, 063307.
(47) Tallaire, A.; Rond, C.; Benedic, F.; Brinza, O.; Achard, J.; Silva, F.; Gicquel, A. Effect of Argon Addition on the Growth of Thick Single Crystal Diamond by High-Power Plasma CVD. *Phys. Status Solidi A* **2011**, *208*, 2028−2032.
(48) Sharma, R.; Woehrl, N.; Vrucinic, M.; Timpner, M.; Buck, V.; Barhai, P. K. Effect of Microwave Power and C_2 Emission Intensity on Structural and Surface Properties of Nanocrystalline Diamond Films. *Thin Solid Films* **2011**, *519*, 7632−7637.
(49) Vlcek, J.; Fendrych, F.; Taylor, A.; Novotny, M.; Liehr, M. Pulsed Plasmas Study of Linear Antennas Microwave CVD System for Nanocrystalline Diamond Film Growth. *J. Mater. Res.* **2012**, *27*, 863−867.
(50) Gicquel, A.; Derkaoui, N.; Rond, C.; Benedic, F.; Cicala, G.; Moneger, D.; Hassouni, K. Quantitative Analysis of Diamond Deposition Reactor Efficiency. *Chem. Phys.* **2012**, *398*, 239−247.
(51) Richley, J. C.; Kelly, M. W.; Ashfold, M. N. R.; Mankelevich, Y. A. Optical Emission from Microwave Activated C/H/O Gas Mixtures for Diamond Chemical Vapor Deposition. *J. Phys. Chem. A* **2012**, *116*, 9447−9458.
(52) Vikharev, A. L.; Gorbachev, A. M.; Muchnikov, A. B.; Radishev, D. B.; Kopelovich, E. A.; Troitskiy, M. M. Investigation of the Optimized Parameters of Microwave-Plasma-Assisted Chemical Vapour Deposition Reactor Operation in a Pulsed Mode. *J. Phys. D: Appl. Phys.* **2012**, *45*, 395202.
(53) Derkaoui, N.; Rond, C.; Hassouni, K.; Gicquel, A. Spectroscopic Analysis of H_2/CH_4 Microwave Plasma and Fast Growth Rate of Diamond Single Crystal. *J. Appl. Phys.* **2014**, *115*, 233301.
(54) Linnik, S.; Gaydaychuk, A. Application of Optical Emission Spectroscopy for the Determination of Optimal CVD Diamond Growth Parameters in Abnormal Glow Discharge Plasma. *Vacuum* **2014**, *103*, 28−32.
(55) Cao, W.; Ma, Z.-B. Optical Spectroscopy for High-Pressure Microwave Plasma Chemical Vapor Deposition of Diamond Films. *Spectrosc. Spectral Anal.* **2015**, *35*, 3007−3011.
(56) Hemawan, K. W.; Hemley, R. J. Optical Emission Diagnostics of Plasmas in Chemical Vapor Deposition of Single-Crystal Diamond. *J. Vac. Sci. Technol., A* **2015**, *33*, 061302.
(57) Bolshakov, A. P.; Ralchenko, V. G.; Yurov, V. Y.; Popovich, A. F.; Antonova, I. A.; Khomich, A. A.; Ashkinazi, E. E.; Ryzhkov, S. G.; Vlasov, A. V.; Khomich, A. V. High-rate growth of single crystal diamond in microwave plasma in CH_4/H_2 and $CH_4/H_2/Ar$ gas mixtures in presence of intensive soot formation. *Diamond Relat. Mater.* **2016**, *62*, 49−57.
(58) Rond, C.; Salem, R.; Hamann, S.; Lombardi, G.; Röpcke, J.; Gicquel, A. Chemical Analysis of H_2/B_2H_6 and $H_2/CH_4/B_2H_6$ Microwave CVD Plasmas used for Diamond Deposition. *Plasma Sources Sci. Technol.* **2016**, *25*, 025016.
(59) Truscott, B. S.; Kelly, M. W.; Potter, K. J.; Ashfold, M. N. R.; Mankelevich, Y. A. Microwave Plasma Enhanced Chemical Vapour Deposition of Nitrogen Doped Diamond, II: $CH_4/N_2/H_2$ plasmas. *J. Phys. Chem. A* **2016**, *120*, 8537−8549.
(60) Mankelevich, Yu.A.; Ashfold, M. N. R.; Ma, J. Plasma-Chemical Processes in Microwave Plasma Enhanced Chemical Vapour Deposition Reactors Operating with C/H/Ar Gas Mixtures. *J. Appl. Phys.* **2008**, *104*, 113304.
(61) Hassouni, K.; Silva, F.; Gicquel, A. Modelling of Diamond Deposition Microwave Cavity Generated Plasmas. *J. Phys. D: Appl. Phys.* **2010**, *42*, 153001 and references therein..
(62) Stoner, B. R.; Ma, G. H. M.; Wolter, S. D.; Glass, J. T. Characterization of Bias-Enhanced Nucleation of Diamond on Silicon by In Vacuo Surface-Analysis and Transmission Electron-Microscopy. *Phys. Rev. B: Condens. Matter Mater. Phys.* **1992**, *45*, 11067−11084.
(63) Saito, D.; Isshiki, H.; Kimura, T. Positive-Bias Enhanced Growth of High Quality Diamond Films by Microwave Plasma Chemical Vapor Deposition. *Diamond Relat. Mater.* **2009**, *18*, 56−60.
(64) Ma, J.; Richley, J. C.; Ashfold, M. N. R.; Mankelevich, Yu.A. Probing the Plasma Chemistry in a Microwave Reactor used for Diamond Chemical Vapour Deposition by Cavity Ring Down Spectroscopy. *J. Appl. Phys.* **2008**, *104*, 103305.
(65) Brooke, J.; Bernath, P.; Schmidt, T.; Bacskay, G. Line Strengths and Updated Molecular Constants for the C_2 Swan System. *J. Quant. Spectrosc. Radiat. Transfer* **2013**, *124*, 11−20.

DOI: 10.1021/acs.jpca.7b00814
J. Phys. Chem. A 2017, 121, 2760−2772

(66) Western, C. M. *PGOPHER*, a Program for Rotational, Vibrational and Electronic Spectra (version 9.0, 2015), University of Bristol. Available at http://pgopher.chm.bris.ac.uk/.
(67) Herzberg, G.; Lagerqvist, A. A New Spectrum Associated with Diatomic Carbon. *Can. J. Phys.* **1968**, *46*, 2363−2373.
(68) Jones, P. L.; Mead, R. D.; Kohler, B. E.; Rosner, S. D.; Lineberger, W. C. Photodetachment Spectroscopy of C_2^- Autodetaching Resonances. *J. Chem. Phys.* **1980**, *73*, 4419−4432.
(69) Leutwyler, S.; Maier, J.; Misev, L. Lifetimes of C_2 in Rotational Levels of the $B^2\Sigma^+_u$ State in the Gas Phase. *Chem. Phys. Lett.* **1982**, *91*, 206−208.
(70) Cathro, W. S.; Mackie, J. C. Oscillator Strength of the C_2^- $B^2\Sigma$−$X^2\Sigma$ Transition: A Shock-Tube Determination. *J. Chem. Soc., Faraday Trans. 2* **1973**, *69*, 237−245.
(71) Kelly, M. W.; Richley, J. C.; Western, C. M.; Ashfold, M. N. R. Exploring the Plasma Chemistry in Microwave Chemical Vapor Deposition of Diamond from C/H/O Gas Mixtures. *J. Phys. Chem. A* **2012**, *116*, 9431−9446.
(72) Ervin, K. M.; Lineberger, W. C. Photoelectron-Spectra of C_2^- and C_2H^-. *J. Phys. Chem.* **1991**, *95*, 1167−1177.
(73) Caledonia, G. E. A Survey of the Gas-Phase Negative Ion Kinetics of Inorganic Molecules: Electron Attachment Reactions. *Chem. Rev.* **1975**, *75*, 333−351.
(74) Andersen, L. H.; Hvelplund, P.; Kella, D.; Moklery, P. H.; Pedersen, H. B.; Schmidt, H. T.; Vejby-Christensen, L. Resonance Structure in the Electron-Impact Detachment Cross Section of C_2^- Caused by the Formation of C_2^{2-}. *J. Phys. B: At., Mol. Opt. Phys.* **1996**, *29*, L643−L649.
(75) Vuitton, V.; Lavvas, P.; Yelle, R. V.; Galand, M.; Wellbrock, A.; Lewis, G. R.; Coates, A. J.; Wahlun, J. E. Negative Ion Chemistry in Titan's Upper Atmosphere. *Planet. Space Sci.* **2009**, *57*, 1558−1572.
(76) May, O.; Fedor, J.; Ibănescu, B. C.; Allan, M. Absolute Cross Sections for Dissociative Electron Attachment to Acetylene and Diacetylene. *Phys. Rev. A: At., Mol., Opt. Phys.* **2008**, *77*, 040701.
(77) Szymańska, E.; Čadež, I.; Krishnakumar, E.; Mason, N. J. Electron Impact Induced Anion Production in Acetylene. *Phys. Chem. Chem. Phys.* **2014**, *16*, 3425−3432.
(78) Barckholtz, C.; Snow, T. P.; Bierbaum, V. M. Reactions of C_n^- and C_nH^- with Atomic and Molecular Hydrogen. *Astrophys. J.* **2001**, *547*, L171−L174.
(79) Locht, R. Mass Spectrometric Investigation of the Appearance of Negative Ions by Dissociative Electron Attachment in Polyatomic Molecules. *Bull. de la Classe des Sciences, Académie Royale de Belgique* **1970**, *LVI*, 788−817.
(80) Pasternack, L.; Pitts, W. M.; McDonald, J. R. Temperature Dependence of Reactions and Intersystem Crossing of $C_2(a^3\Pi_u)$ with Hydrogen and Small Hydrocarbons from 300−600 K. *Chem. Phys.* **1981**, *57*, 19−28.
(81) Sander, R. K.; Tiee, J. J.; Quick, C. R.; Romero, R. J.; Estler, R. Quenching of C_2H Emission Produced by Vacuum Ultraviolet Photolysis of Acetylene. *J. Chem. Phys.* **1988**, *89*, 3495−3501.
(82) Wang, H. L.; Zhu, Z. Q.; Zhang, S. H.; Pei, L. S.; Chen, Y. Time-Resolved Kinetic Studies on Quenching of $C_2(d^3\Pi_g)$ by Alkanes and Substituted Methane Molecules. *Chem. Phys. Lett.* **2005**, *407*, 217−221.
(83) Fortov, V. E., Ed. *Encyclopedia of Low Temperature Plasma*; Nauka: Moscow, 2000; Vol. *1*, Section I.2.6.
(84) Kuchitsu, K., Ed. *Structure of Free Polyatomic Molecules − Basic Data*; Springer-Verlag: Berlin, 1998.
(85) Truscott, B. S.; Kelly, M. W.; Potter, K. J.; Johnson, M.; Ashfold, M. N. R.; Mankelevich, Yu.A. Microwave Plasma Enhanced Chemical Vapour Deposition of Nitrogen Doped Diamond, I: N_2/H_2 and NH_3/H_2 Plasmas. *J. Phys. Chem. A* **2015**, *119*, 12962−76.
(86) Mironovich, K. V.; Mankelevich, Yu. A.; Voloshin, D. G.; Dagesjan, S. A.; Krivchenko, V. A.. Modeling and Optical Spectroscopy of DC Discharge in CH_4/H_2 Mixture for Nanostructured Carbon Films. *Plasma Physics Reports*. 2017, *43*, in press.
(87) Aleksandrov, N. L. Three-Body Electron Attachment to a Molecule. *Usp. Fiz. Nauk* **1988**, *154*, 177−206.
(88) Bradforth, S. E.; Kim, E. H.; Arnold, D. W.; Neumark, D. M. Photoelectron Spectroscopy of CN^-, NCO^- and NCS^-. *J. Chem. Phys.* **1993**, *98*, 800−810.
(89) May, O.; Kubala, D.; Allan, M. Absolute Cross Sections for Dissociative Electron Attachment to HCN and DCN. *Phys. Rev. A* **2010**, *82*, 010701R.
(90) The UMIST Database for Astrochemistry 2012. http://udfa.ajmarkwick.net/.
(91) Robertson, J.; Gerber, J.; Sattel, S.; Weiler, M.; Jung, K.; Ehrhardt, H. Mechanism of Bias-Enhanced Nucleation of Diamond on Si. *Appl. Phys. Lett.* **1995**, *66*, 3287−3289.
(92) Ma, Y.; Tsurumi, T.; Shinoda, N.; Fukunaga, O. Effect of Bias Enhanced Nucleation on the Nucleation Density of Diamond in Microwave Plasma CVD. *Diamond Relat. Mater.* **1995**, *4*, 1325−1330.
(93) Kulisch, W.; Ackermann, L.; Sobisch, W. On the Mechanisms of Bias Enhanced Nucleation of Diamond. *Phys. stat. Sol. (a)* **1996**, *154*, 155−174.
(94) Stockel, R.; Stammler, M.; Janischowsky, K.; Ley, L.; Albrecht, M.; Strunk, H. P. Diamond Nucleation Under Bias Conditions. *J. Appl. Phys.* **1998**, *83*, 531−539.

DOI: 10.1021/acs.jpca.7b00814
J. Phys. Chem. A 2017, 121, 2760−2772